Chemical Engineering Journal 449 (2022) 137802

Contents lists available at ScienceDirect

Chemical Engineering Journal

journal homepage: www.elsevier.com/locate/cej

Targeted construction of a three-dimensional metal covalent organic framework with spn topology for photocatalytic hydrogen peroxide production

Wang-Kang Han [a], Hui-Shu Lu [a], Jia-Xing Fu [a], Xin Liu [a], Xiangmiao Zhu [a], Xiaodong Yan [a], Jiangwei Zhang [b,*], Yuqin Jiang [c], Hongliang Dong [d], Zhi-Guo Gu [a,*]

[a] Key Laboratory of Synthetic and Biological Colloids, Ministry of Education, School of Chemical and Material Engineering, Jiangnan University, Wuxi 214122, China
[b] College of Chemistry and Chemical Engineering, Inner Mongolia University, Hohhot 010021, China
[c] Henan Engineering Research Centre of Chiral Hydroxyl Pharmaceutical, School of Chemistry and Chemical Engineering, Henan Normal University, Xinxiang 453007, China
[d] Center for High Pressure Science and Technology Advanced Research, Shanghai 201203, China

ARTICLE INFO

Keywords:
Covalent organic frameworks
Three-dimensional
Photocatalysis
Hydrogen peroxide production

ABSTRACT

To enrich the topology of three-dimensional covalent organic frameworks (3D COFs) is an appealing challenge. Till now, only 20 types of topologies have been achieved in 3D COFs because of the limited polyhedral building blocks. Herein, we report the first 3D titanium-based COF with **spn** topology (TiCOF-spn) through [6 + 3] imine condensation of a Ti(IV) complex with six aldehyde groups positioned in a trigonal antiprismatic arrangement and a planar triazine-based amine connector. Interestingly, TiCOF-spn contains two kinds of pores, that is, the linking of the tetrahedral cages by sharing vertices forms the truncated tetrahedral cages. By integrating the crystalline porous framework, photoactive titanium center and triazine component, TiCOF-spn shows strong visible light absorption and efficient photocatalytic activity for producing H_2O_2 (489.94 μmol $g^{-1}h^{-1}$). This work expands the topology of the 3D COFs family and pioneers the application of metal-containing COFs in solar energy conversion.

1. Introduction

Covalent organic frameworks (COFs) are the most intriguing crystalline organic porous materials because of their structural and functional versatility, and potential applications in gas adsorption/separation, heterogeneous catalysis, energy conversion, *etc* [1–7]. Over the past decade, two-dimensional (2D) COFs with layered structures have witnessed rapid increase in this area [8–10]. In contrast, the structural diversity of 3D COFs are extremely confined due to the lack of polyhedral stereoscopic molecular building units and the difficulty in crystallization [11,12]. To date, only 20 types of topologies (**ctn** [13], **bor** [13], **dia** [14], **pts** [15], **rra** [16], **ffc** [17], **srs** [18], **lon** [19], **stp** [20], **acs** [21] **fjh** [22], **tbo** [23], **bcu** [24], **ceq** [25], **ljh** [26], **soc** [27], **pcu** [28], **nbo** [29], **hea** [30] and **pcb** [31]) have been realized in 3D COFs. The longstanding challenge, therefore, is the exploration of novel topologies to expand the 3D COFs family.

The key to designing and synthesizing a specific COF is the selection of building units with appropriate geometry. For example, a **dia** network requires linear linkers and tetrahedral nodes ($T_d + C_2$) [14], while a **pts** topology relies on quadrilateral and tetrahedral building units ($T_d + C_2$ or C_4) [15]. Notably, the implement of high-connectivity is an attractive step to unlock new topologies and increase structural diversity in 3D COFs. Recently, the 6-connected triangular prism building units were used to construct new architectures with **acs** ($D_{3h} + C_2$) [21], **ceq** ($D_{3h} + C_3$)[25] and **stp** ($D_{3h} + C_4$) [20] topologies. Similarly, the trigonal antiprisms (D_3) can also be viewed as 6-connected polyhedrons, and the functionalized vertexes of these polyhedrons can link up with other suitable nodes to form framework structures with the potential for new topologies. However, this kind of building unit has been rarely utilized for the synthesis of 3D COFs. According to the Reticular Chemistry Structure Resource (RCSR) database [32], only limited topologies (**ant**, **apo**, **cep**, **pyr**, **rtl, tsx**, **eea** and **spn**) can be formed by the combination

* Corresponding authors at: Key Laboratory of Synthetic and Biological Colloids, Ministry of Education, School of Chemical and Material Engineering, Jiangnan University, Wuxi 214122, China (Z.-G. Gu). College of Chemistry and Chemical Engineering, Inner Mongolia University, Hohhot 010021, China (J. Zhang).
E-mail addresses: zjw11@tsinghua.org.cn (J. Zhang), zhiguogu@jiangnan.edu.cn (Z.-G. Gu).

https://doi.org/10.1016/j.cej.2022.137802
Received 13 April 2022; Received in revised form 22 June 2022; Accepted 25 June 2022
Available online 27 June 2022

of trigonal antiprismatic and triangular building units (Fig. S1). We found that these topologies could be divided into two types: (i) **ant**, **apo**, **cep**, **pyr**, **rtl** and **tsx** with "compressed" trigonal antiprismatic node, (ii) **eea** and **spn** with "elongated" trigonal antiprismatic node. After narrowing down the range of possible topologies by using "elongated" trigonal antiprismatic node, we pay close attention to targeted constructing new 3D COFs with **eea** or **spn** topologies (Fig. 1a). Nevertheless, the synthesis of "elongated" trigonal antiprism organic building units is a daunting task.

Notably, trigonal antiprism polyhedrons are common in metal complexes, which strongly encourage us to employ metal-containing precursor as building unit for designing and synthesizing 3D COFs. In this research, we start with an aldehyde functionalized Ti(IV) catecholate complex $Na_2Ti(2,3\text{-}DHTA)_3$ (2,3-DHTA = 2,3-dihydroxyterephthalaldehyde). It has been proved that this titanium building unit can serve as a 6-connected starting point for constructing the first 3D **soc** COF in our group previously [27]. After carefully analyzing the X-ray single crystal structure of $Na_2Ti(2,3\text{-}DHTA)_3$ again, it is discovered that the spatial orientation of the six aldehyde groups adopts a distorted and elongated trigonal antiprismatic feature since the angular parameters ϕ and θ equal to 31° and 49°, respectively (Fig. 1a and Fig. S2). It suggests that $Na_2Ti(2,3\text{-}DHTA)_3$ is a promising candidate for synthesizing 3D COFs with **eea** or **spn** topologies. With this in mind, a new titanium-based COF, namely TiCOF-spn, was synthesized by condensation of $Na_2Ti(2,3\text{-}DHTA)_3$ and a planar amine linker 1,3,5-tris(4-aminophenyl) triazine (TAPT). Multiple techniques such as powder X-ray diffraction measurement (PXRD) and structural simulations, pair-distribution function (PDF) and X-ray absorption fine structure (XAFS) analysis were then combined to completely characterize the topology and structure of TiCOF-spn. The crystalline porous structure, photoactive titanium center and triazine unit of TiCOF-spn further inspired us to explore its heterogeneous photocatalysis.

2. Experimental

A complete description of chemicals, materials, and instrumentations is available in the Supporting Information.

2.1. Synthesis of TiCOF-spn

The TiCOF-spn was synthesized by solvothermal condensation reaction. $Na_2Ti(2,3\text{-}DHTA)_3$ (11.72 mg, 0.02 mmol) and TAPT (14.2 mg, 0.04 mmol) were dissolved in a mixed solvent of 0.6 mL *o*-dichlorobenzene, 0.6 mL mesitylene, 0.3 mL acetonitrile and 0.15 mL 6 M aqueous acetic acid in a pyrex tube. This mixture was sonicated for 10 min to obtain a homogeneous dispersion. Then, the pyrex tube was flash frozen in a liquid N_2 bath and degassed by freeze–pumpthaw technique for three times and sealed under vacuum. Upon warmed to room temperature, the tube was placed in an oven and heated at 120 °C for 7 days. The precipitate was collected by filtration, washed with DMF (8 × 5 mL), extracted by soxhlet extractor with tetrahydrofuran for 24 h, and finally dried at 120 °C under vacuum for 12 h to obtain TiCOF-spn as brown crystalline powder (72%). Elemental analysis of TiCOF-spn: Calcd for $Na_8Ti_4O_{24}C_{264}H_{144}N_{48}$: C, 66.78%; H, 3.06%; N, 14.16%. Found: C, 66.92%; H, 3.25%; N, 14.01%.

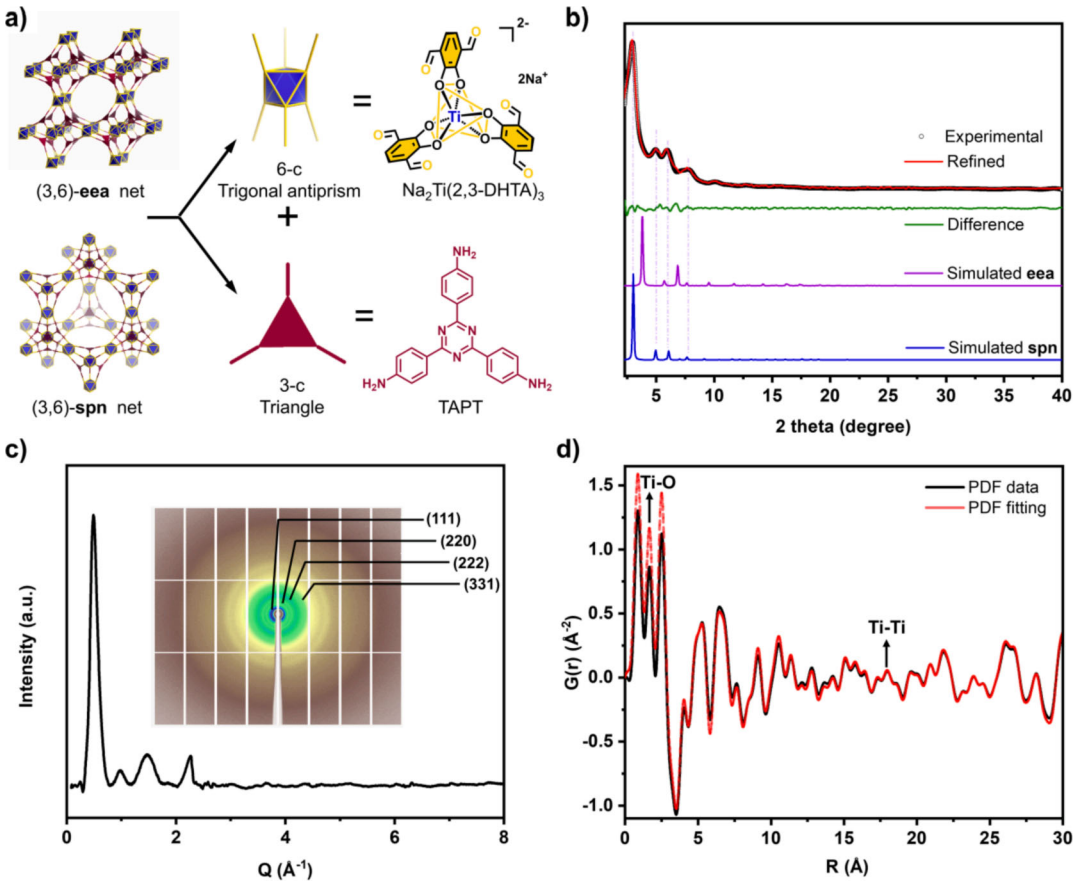

Fig. 1. (a) Representation of the (3,6)-connected eea and spn topologies, which were deconstructed into trigonal antiprismatic and planar triangle linkers with their corresponding chemical equivalents $Na_2Ti(2,3\text{-}DHTA)_3$ and TAPT. (b) The experimental (black) and Pawley refined (red) PXRD patterns of TiCOF-spn, the difference between the experimental and refined PXRD patterns (green), and the simulated PXRD patterns based on eea net (purple) and spn net (blue). (c) The 2D scattering image of TiCOF-spn was reduced to 1D data. (d) The PDF data and calculated PDF pattern with spn net for TiCOF-spn.

2.2. Photocatalysis experiment

Hydrogen peroxide (H_2O_2) production was carried out in a photocatalytic reactor (PerfectLight). In detail, 40 mg photocatalyst was dispersed in 120 mL solution and sonicated for 2 min to form a homogeneous suspension. The resulting mixture was bubbled with oxygen gas in the dark for 30 min to obtain an oxygen equilibrated environment. The oxygen bubbling was continued during the photocatalytic reaction. Subsequently, the suspension was irradiated under a 300 W Xe lamp with a 420 nm cutoff filter to imitate visible light irradiation (420 nm $\leq \lambda \leq$ 780 nm). The temperature was maintained at 25 °C using a condenser.

The concentration of H_2O_2 was determined by iodometric method. Typically, solution A was prepared by mixing solutions B and C equal in weight. Solution B was prepared by dissolving 16.5 g KI, 0.5 g NaOH and 0.05 g of ammonium molybdate tetrahydrate in 250 mL ultrapure water. Solution C was prepared by dissolving 5 g KHP in 250 mL ultrapure water. 1.5 mL reaction solution that was taken at a certain time during the irradiation and filtered through a 0.22 um membrane filter. The filtrate was added into 1.5 mL solution A. After standing for 15 min, extra 14.0 mL ultrapure water was added into the mixture to dilute the solution. Finally, the concentration of H_2O_2 was immediately detected by UV/vis absorption at $\lambda = 352$ nm. The reported data is the average of three parallel experiments.

3. Result and discussion

3.1. Synthesis and characterization

To implement our idea, the $Na_2Ti(2,3\text{-DHTA})_3$ was reacted with various 3-connected amines via [6 + 3] imine condensation. However, most of them resulted in amorphous products although we tried a wide range of synthetic conditions except for 1,3,5-tris(4-aminophenyl) triazine (TAPT). The crystalline product (TiCOF-spn) could be obtained through the condensation of $Na_2Ti(2,3\text{-DHTA})_3$ and TAPT in a mixture solvent of *o*-dichlorobenzene, mesitylene and acetonitrile with 6 M acetic acid as the catalyst at 120 °C for 7 days. The Fourier transform infrared (FTIR) spectrum of TiCOF-spn displayed a new absorption peak at 1626 cm^{-1} attributed to C = N bonds, with no identifiable aldehyde (1660 cm^{-1}) and amine (3319 cm^{-1}) stretches remaining, indicating the complete imine condensation (Fig. S5). TiCOF-spn was stable in different solvents, such as THF, DMF, DMSO, MeOH, 1 M HCl and 1 M NaOH aqueous solutions (Fig. S6-S8). Thermogravimetric analysis also showed that TiCOF-spn was thermally stable up to about 350 °C (Fig. S9). It was further verified by the ^{13}C cross-polarization magic-angle-spinning (CP/MAS) NMR, showing typical C = N resonance signal at 163 ppm (Figs. S10 and S11). The fitted O 1 s in X-ray photoelectron spectroscopy (XPS) spectrum demonstrated the presence of the Ti-O (531.4 eV) and C-O bonds (533.2 eV), while two distinct peaks of Ti $2p_{1/2}$ and Ti $2p_{3/2}$ at 464.2 and 458.4 eV still belong to the Ti-O bonds (Fig. S12).

To elucidate the crystalline nature and have a deep view of the structural information of TiCOF-spn, PXRD measurement accompanied with theoretical simulation was conducted. As shown in Fig. 1b, the experimental PXRD pattern exhibited diffraction peaks at 3.0°, 5.0°, 5.9° and 7.7° which respectively correspond to the (1 1 1), (2 2 0), (2 2 2) and (3 3 1) facets. The structural model was then built based on **spn** and **eea** net, respectively. The calculated PXRD pattern of the geometrically optimized structure adopting **spn** topology with $F4_132$ space group matches well with the experimental one. The Pawley refinement yielded unit cell parameters of $a = b = c = 50.11$ Å and $\alpha = \gamma = \beta = 90°$ with good agreement factors (R_p = 3.17 % and R_{wp} = 4.75 %). The Rietveld refinement was further carried out to refine the structure of TiCOF-spn, which led to a space group of $F4_132$ with $a = b = c = 49.77$ Å, $\alpha = \gamma = \beta = 90°$ (R_p = 6.31 % and R_{wp} = 9.02 %) (Fig. S13). The Rietveld refinement reproduced the PXRD pattern well. In contrast, the calculated PXRD patterns based on the non-interpenetrated **eea** and the two-fold interpenetrated **spn** topologies for TiCOF-spn were not in agreement with the experimental one (Figs. S14 and S15). Besides, it should be noted that the **spn** net is an edge-transitive topology, while the **eea** net is a non-edge-transitive topology. As a rule of thumb, the edge-transitive nets are the most likely products to form [33]. Consequently, all the above results suggest that a non-interpenetrated structure based on **spn** net is reasonable for TiCOF-spn.

To further probe the structure of TiCOF-spn, synchrotron radiation X-ray total scattering with PDF analysis was performed. The PDF technique can provide information about structural correlations in a material, and intuitively gives the probability to find pairs of atoms separated by a distance *r*, making this technique useful for the characterization of 3D COFs with new topologies [34,35]. The crystalline nature of TiCOF-spn is again confirmed by the reduced 1D scattering signal at 0.49 $Å^{-1}$, 0.98 $Å^{-1}$, 1.47 $Å^{-1}$, 2.26 $Å^{-1}$, which are assignable to the (1 1 1), (2 2 0), (2 2 2) and (3 3 1) facets (Fig. 1c). Long distance oscillations peaks before the signal damp to zero in the PDF also suggest the ordered architecture (Fig. 1d). The notable peaks in the PDF at 1.7 and 17.9 Å correspond to the Ti-O and Ti-Ti distances in TiCOF-spn, which are consistent with the theoretical values (1.9 Å for Ti-O and 17.7 Å for Ti-Ti). Besides, the PDF calculated result for the optimized structure model with **spn** net matches well with the experimental data, and further confirms the 3D structure of TiCOF-spn.

In TiCOF-spn, each Ti(IV) complex $Ti(2,3\text{-DHTA})_3^{2-}$ is connected to six TAPT, and each of TAPT is covalently linked to three $Ti(2,3\text{-DHTA})_3^{2-}$, with Na^+ ion balancing the charge. The spatially oriented connection of the building units also led to the formation of two types of polyhedral cages in TiCOF-spn, that is the tetrahedral cage A (Fig. 2a) and truncated tetrahedral cage B (Fig. 2b) with 15.1 Å and 28.1 Å in cavity size, respectively. Each planar TAPT linker covers one face of the tetrahedral cage A, while each corner of the tetrahedron is occupied by a $Ti(2,3\text{-DHTA})_3^{2-}$ unit. In the truncated tetrahedral cage B, 12 $Ti(2,3\text{-DHTA})_3^{2-}$ occupy the vertexes, while 12 TAPT linkers serve as the sides and another 4 TAPT linkers cover the trigonal faces, giving a face symbol of [12^4]. The truncated tetrahedral cage B links 10 tetrahedral cage A by sharing vertices and trigonal faces, resulting in the TiCOF-spn (Fig. 2c). Specifically, cages B are connected with each other in "window to window" manner to form open channels (Fig. 2d). On the other hand, the structure of TiCOF-spn can be understood from an interlocking perspective. In detail, four individual 2D covalently linked hexagonal grids with **hcb** topology are intertwined along the faces of the

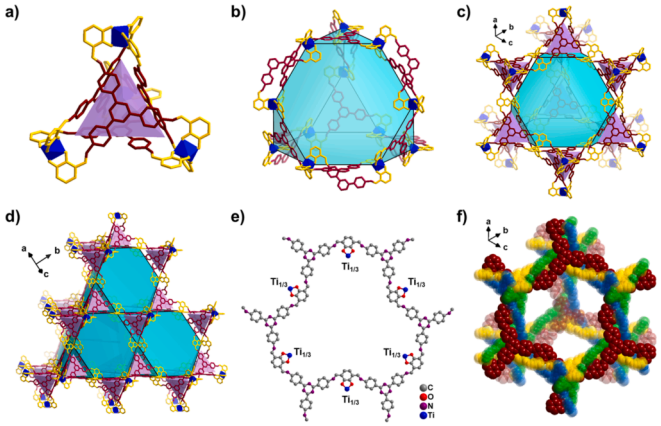

Fig. 2. The structure of TiCOF-spn: (a) tetrahedral cage A (purple cavity), (b) truncated tetrahedral cage B (blue cavity), and (c) the spn topology showing one cage B surrounded by ten cage A. (d) The truncated tetrahedral cavities are interconnected to form 3D channel. (e) The structure of 2D hexagonal grid. (f) The space filling representation of TiCOF-spn illustrating the interlocking of 2D hexagonal grids to form the 3D framework structure. The 2D grids were coloured separately for clarity.

tetrahedron, and further anchored by the coordination effect between Ti (IV) metal ions and oxygen atoms at the vertices of the tetrahedron, resulting in the 3D framework with **spn** topology (Fig. 2e and 2f). Noteworthily, TiCOF-spn is different from the well-known metal organic frameworks (MOFs) which are built from metal ions joined by organic linkers through metal–ligand coordination bonds. MOFs do not have covalently linked networks due to the metal ions nodes. By contrast, the organic components are connected by reversible imine linkages to form four 2D covalent networks in TiCOF-spn, meanwhile the Ti(IV) metal ions further contribute to constructing the framework to increase the dimensionality of TiCOF-spn from 2D to 3D. Similarly, weaving of organic threads and interlocking of 1D square ribbons into crystalline COFs have recently been reported starting from copper complexes building unit. In these cases, the metal ions serve as points to guide the organic molecular units covalently linked in a defined direction thus forming 3D covalent frameworks [2,36–39]. With these taken into consideration, TiCOF-spn can be classified as a COF. Consequently, TiCOF-spn is an unprecedented example of 3D **spn** COF, and exhibits the assembly of polyhedral cages, thus leading to porous framework feature.

The XAFS at the Ti K-edge of TiCOF-spn and the corresponding Ti foil, TiC and TiO_2 references were performed to further verify the valance state and coordination environment of Ti atoms. As shown in the X-ray absorption near edge structure (XANES) spectra (Fig. 3a), the Ti in the TiCOF-spn showed a positive shift of the absorption edge position, while overlapping the position of TiO_2, indicating an oxidation state approaching Ti^{4+} in TiCOF-spn. The obvious scattering path signals of Ti-O bonds in first coordination shell located at 1.72 Å and Ti-O-C bonds in second coordination shell located at 2.96 Å from the radial distance space spectra χ(R) for Ti K-edge of TiCOF-spn suggested that the existence of TiO_6 coordination geometry (Fig. 3b). Moreover, the wavelet transforms of χ(k) further demonstrated the TiO_6 local coordination environment with only scattering path signal of Ti-O located at [χ(k), χ(R)] of [5.2, 1.76] being observed (Fig. 3c). Quantitative χ(R) space spectra fitting were then performed with the consideration of the first and the second coordination shell. It showed that the coordination numbers (CN) were approaching 6.0 for both of Ti-O bonding [CN = N*amp = 6.0*(1.01+/-0.12)] at 1.95 Å and Ti-O-C bonding [CN = N*amp = 6.0*(0.80+/-0.12)] at 2.96 Å (Table S1). The good fitting results of χ(R) and χ(k) space spectra further supported the local structure and atomically dispersed state of TiO_6 linking cluster in TiCOF-spn (Fig. 3d and 3e).

The porous structure of TiCOF-spn was analyzed by N_2 and Ar adsorption–desorption measurements, respectively (Fig. S16). It exhibited a type IV isotherms, indicating the mesoporous characteristics. The N_2 and Ar Brunauer-Emmett-Teller (BET) surface areas were calculated to be 621.38 $m^2\ g^{-1}$ and 564.26 $m^2\ g^{-1}$, respectively, which are lower than the theoretical Connolly surface (3029 $m^2\ g^{-1}$) of the anion framework. This may be due to the internal pores that are occupied by the balance charges (solvated Na^+ ion), and the surface channels are blocked to a certain extent by some small COF nanoparticles. The pore size distribution calculated by nonlocal density functional theory showed two kinds of pores of 1.41 and 2.70 nm by N_2 measurement (1.48 and 2.63 nm by Ar measurement) (Fig. S16b and d), which were consistent with the theoretical ones (15.1 and 28.1 Å). Additionally, the porosity was further corroborated by the dye uptake experiments (Figs. S17–S29). The TiCOF-spn showed significant adsorption towards cationic and neutral dye (rhodamine B, methylene blue and neutral red), while displayed less uptake over anionic dye methyl orange. The remarkable charge selectivity confirmed the anionic skeleton of TiCOF-spn. EDAX analysis was carried out to quantify the amounts of Ti and Na in TiCOF-spn (Fig. S30), which further proved the anionic skeleton.

The scanning electron microscope (SEM) and transmission electron microscope (TEM) images revealed a follower-like morphology of TiCOF-spn, which was likely comprised of many polyhedron crystals (Fig. 4a and 4b). The high-resolution TEM image was taken to reveal the crystallinity and network (Fig. 4c). The zoom-in inset showed the reticular structure with approximately hexagonal pores with a size of ~ 2.52 nm. The observed pore size was close to the theoretical one of cage B. The dislocation diagram obtained by inverse Fourier transform showed clear reticular structure, which also matched well with the **spn** topology (Fig. 4d). Further, the EDS elemental mapping analysis exhibited the uniform elemental distribution of C, N, O and Ti in TiCOF-spn (Fig. 4e). The accurate content of Ti element was further determined by ICP-OES to be 3.86 wt%, which is close to the theoretical value of 4.03 wt%.

3.2. *Photocatalytic production of H_2O_2*

TiCOF-spn shares characteristics of COFs and MOFs as it is covalently connected, titanium-based crystalline material. Herein, TiCOF-spn was further explored for photocatalytic applications. And the optical and electronic properties of TiCOF-spn was firstly investigated.

As shown in Fig. 5a and 5b, the broad absorption and low optical band gap (E_g = 1.95 eV) indicate that TiCOF-spn is suitable for visible light harvesting and conversion. It is also showed a ligand-to-metal charge transfer (LMCT) at around 460 nm, indicating the potential photoexcited state. The valence band (E_{VB}) was determined to be 1.68 eV (vs E_F) according to XPS valence band spectrum (Fig. 5c), while the

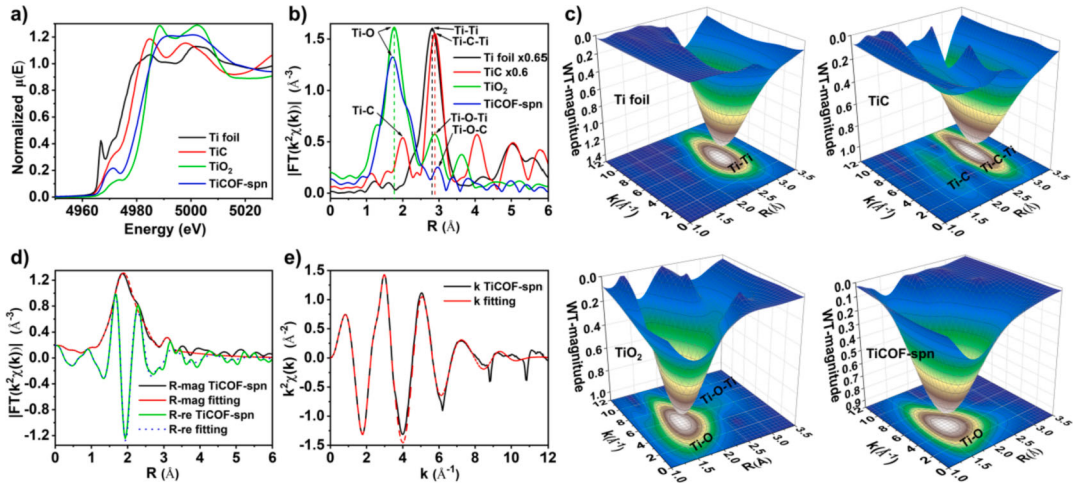

Fig. 3. (a) The normalized XANES μ(E) spectra, (b) the radial distance χ(R) spectra and (c) the 3D contour Wavelet transform extended X-ray absorption fine structure (WTEXAFS) map with 2D projection for Ti K-edge of TiCOF-spn with the corresponding reference: the Ti foil, TiC and TiO_2 as reference, respectively. (d) The χ(R) space spectra fitting curve and (d) the k^2χ(k) space spectra fitting curve for Ti K-edge of TiCOF-spn.

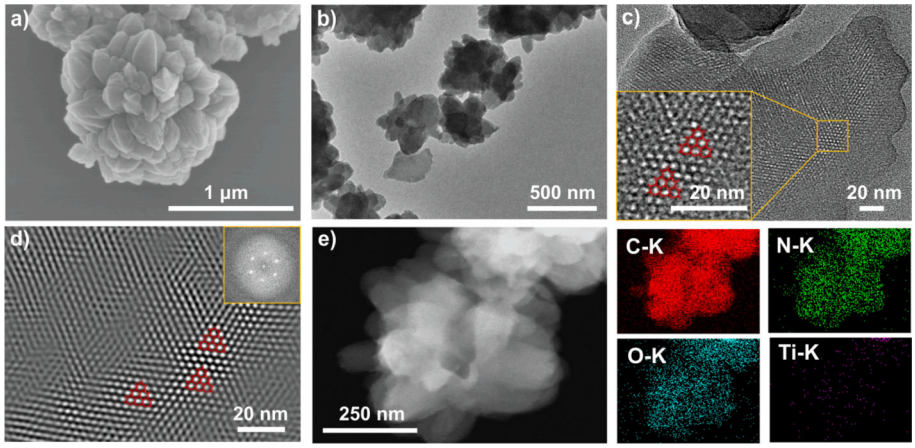

Fig. 4. (a) SEM and (b-c) TEM images of TiCOF-spn. The inset in (c) is the zoom-in of the selected area. (d) Fourier-filtered image of TiCOF-spn. The inset is the corresponding fast Fourier Transform pattern. (e) EDS elemental mapping of TiCOF-spn with C, N, O and Ti elements.

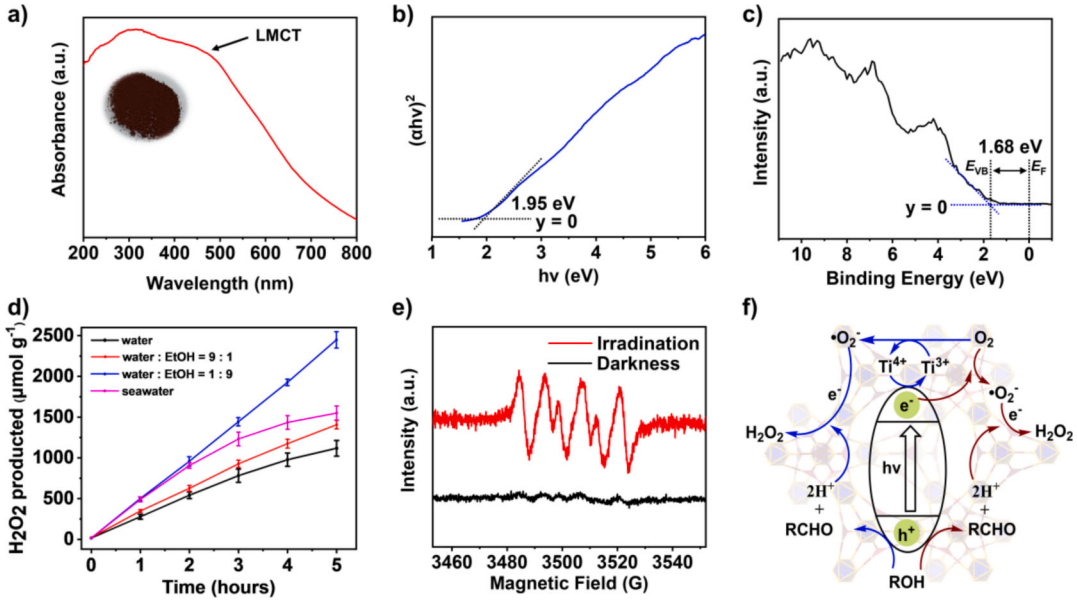

Fig. 5. (a) Solid state UV/vis spectrum. The inset is the corresponding product of TiCOF-spn. (b) Tauc plot analysis for band gap calculation. (c) XPS valence band spectrum of TiCOF-spn. The energy of the E_{VB} is relative to the Fermi level (E_F) located at 0 eV. (d) Time dependent H_2O_2 production under visible light irradiation for TiCOF-spn (40 mg) dispersed in an O_2-saturated solution (120 mL). (e) DMPO spin-trapping EPR spectra of TiCOF-spn under darkness and light. (f) Proposed mechanism for photocatalytic H_2O_2 production catalyzed by TiCOF-spn.

conduction band (E_{CB}) was calculated to be − 0.27 eV (vs E_F). Since the reduction level of oxygen was positioned below the E_{CB}, TiCOF-spn showed potential capability to drive oxygen reduction to H_2O_2 (Fig. S31). To better understand the photoelectochemical properties of TiCOF-spn, transient photocurrent responses and electrochemical impedance spectroscopy (EIS) were conducted. An amorphous material of TiCOF-spn was also synthesized for comparison (Fig. S32). Upon switching the photoirradiation on/off, crystalline TiCOF-spn showed a faster photoresponse with photocurrent density ~0.6 μA cm^{-2}. In contrast, the amorphous counterpart showed a lower photocurrent of ~0.25 μA cm^{-2}. This result indicates that the crystalline structure has more efficient photoinduced charges transfer. Moreover, the much smaller semicircle in EIS further revealed the lower internal charge transfer resistance of crystalline TiCOF-spn than the amorphous counterpart (Fig. S33). H_2O_2 is a valuable chemical having wide applications in the fields of medicine, chemical industry, and environmental management [40–42]. Compared with the traditional approaches, such as anthraquinone method and electrochemical synthesis, photocatalytic H_2O_2 production is more attractive due to its safety and environmental friendliness [43,44].

As shown in Fig. 5d, the production of H_2O_2 continued to increase under the visible light irradiation with TiCOF-spn as the photocatalyst during a period of 5 h. The production rate of H_2O_2 was recorded at 223.55 μmol $g^{-1}h^{-1}$ in the pure water system. Prominently, the H_2O_2 generation rate was increased from 280.33 μmol $g^{-1}h^{-1}$ at a water/ethanol ratio of 9/1 to 489.94 μmol $g^{-1}h^{-1}$ at a water/ethanol ratio of 1/9. This value was superior to the reported TAPD-$(Me)_2$ COF (234.52 μmol $g^{-1}h^{-1}$), and was about four times that of the pure carbon nitride (Table S2). Importantly, H_2O_2 production was enhanced in the seawater (309.98 μmol $g^{-1}h^{-1}$) than in the pure water, indicative of potential solar energy harvesting in seawater. Two main factors are speculated for the improved H_2O_2 production in seawater. Firstly, the presence of metal cations (Na^+, K^+, Mg^{2+}, Ca^{2+}, Sr^{2+}) in seawater can attract more electrons that prolongs the separation time of electron and hole. Secondly, stabilization of $^{\bullet}O_2^-$ through its complexation with a Lewis acid, such as Na^+ ions in seawater, can prevent reaction of $^{\bullet}O_2^-$ and H_2O_2 that

leads to undesired reductive decomposition of H_2O_2 to H_2O. The similar phenomena have also been observed in Ti-containing MOF and organic polymer photocatalysts [45–46]. Moreover, the effect of different alcohol sources (isopropanol and methanol) was also tested by performing the photocatalytic H_2O_2 production (Fig. S35). The increase in the H_2O_2 production rate in the presence of ethanol as sacrificial electron-donor agents suggested that the photocatalytic H_2O_2 production was not from water oxidation by photoinduced holes, since the holes would be consumed by such electron donors. Therefore, the O_2 reduction was the main contribution to the H_2O_2 formation. Besides, it was worthy to note that no H_2O_2 was generated under dark or without TiCOF-spn catalysts, implying that the formation of H_2O_2 was contributed by photocatalysis process. Under N_2 condition, there was also no H_2O_2 detected, demonstrating that the O_2 is essential for H_2O_2 production. This was also confirmed by isotopic labelling experiments using $^{18}O_2$ (Fig. S36). The UV–vis and ICP-OES analyses of the supernatant showed no sign of Ti(IV) complex leaching into the solution during the photocatalysis (Fig. S37). TiCOF-spn can be readily recycled, and its catalytic activity only showed slight change after 5 runs (Fig. S38). The morphologies were still retained after photocatalytic reaction (Fig. S39). The BET surface area was decreased to 316.58 $m^2\ g^{-1}$, which could be attributed to the partial decrease in crystallinity of the recycled TiCOF-spn (Fig. S40 and S41).

Based on the photocatalytic H_2O_2 experimental results, electron paramagnetic resonance (EPR) measurement was carried out to detected the presence of active oxygen species. The 5,5-dimethyl-1-pyrroline-N-oxide (DMPO) spin-trapping EPR spectrum showed six characteristic DMPO-$^{\bullet}O^{2-}$ signals after light illumination, while no signal was observed under darkness (Fig. 5e), illustrating that the single-electron reduction of O_2 to $^{\bullet}O_2^-$ as reaction intermediate in the photocatalytic process. Further, the radical scavenging experiment was carried out with adding the *p*-benzoquinone. It was found that the H_2O_2 production was significantly quenched (Fig. S42). These observations collectively reveal that the H_2O_2 is produced by a sequential two-step single-electron O_2 reduction route, and a possible reaction mechanism is proposed for the photocatalytic H_2O_2 production by TiCOF-spn (Fig. 5f). Upon light irradiation, the photoexcited TiCOF-spn generates the electron-hole pairs. The addition of alcohol can consume the holes to enhance the electron-hole separation and meanwhile provide protons for the H_2O_2 production [47]. The $^{\bullet}O_2^-$ can be produced in two ways. One pathway is the direct reduction of O_2 into $^{\bullet}O_2^-$ by the conduction band e^-. Meanwhile, titanium with inherent variable valence states (Ti^{4+}/Ti^{3+}) and the Ti-mediated electron transfer mechanism through ligand-to-metal charge transfer (LMCT) process has been widely studied [48–50]. Therefore, another one relies on the Ti centers, that is, the Ti^{4+} is reduced to Ti^{3+} by the photoexcited e^-. Then, the electron transferred from Ti^{3+} to O_2 to generate $^{\bullet}O^{2-}$. Finally, the disproportionation of the $^{\bullet}O^{2-}$ forms H_2O_2, which is accelerated by the H^+.

4. Conclusions

In summary, we demonstrated the rational utilization of metal-containing unit to overcome the obstacle of limited polyhedral organic molecular linker for the construction of 3D COFs, and achieved a 3D titanium COF with unreported **spn** topology for photocatalytic H_2O_2 production. Besides, by incorporating metal complex building unit to design and synthesize metal covalent organic framework is an effective approach to establish a bridge between COFs and MOFs. This work thus opens a door to enrich the structures of 3D COFs and promotes the application of COFs in solar energy conversion.

Declaration of Competing Interest

The authors declare that they have no known competing financial interests or personal relationships that could have appeared to influence the work reported in this paper.

Data availability

Data will be made available on request.

Acknowledgment

This work was supported by the National Natural Science Foundation of China (22075108, 21905116, 21701168), the Natural Science Foundation of Jiangsu Province (BK20190614), Dalian High Level Talent Innovation Project (2019RQ063), Open Project Foundation of State Key Laboratory of Structural Chemistry, Fujian Institute of Research on the Structure of Matter, Chinese Academy of Sciences (20200021), and the Open Research Fund of School of Chemistry and Chemical Engineering, Henan Normal University. We are grateful to the support from Central Laboratory, School of Chemical and Material Engineering Jiangnan University. Besides, we gratefully acknowledge BL17B beamline of National Facility for Protein Science (NFPS), Shanghai Synchrotron Radiation Facility (SSRF) Shanghai, China and 1W1B beamline of Beijing Synchrotron Radiation Facility (BSRF) Beijing, China for providing the beam time.

Appendix A. Supplementary data

Supplementary data to this article can be found online at https://doi.org/10.1016/j.cej.2022.137802.

References

[1] C.S. Diercks, O.M. Yaghi, The atom, the molecule, and the covalent organic framework, Science 355 (6328) (2017) eaal1585.
[2] Y. Liu, Y. Ma, Y. Zhao, X. Sun, F. Gándara, H. Furukawa, Z. Liu, H. Zhu, C. Zhu, K. Suenaga, P. Oleynikov, A.S. Alshammari, X. Zhang, O. Terasaki, O.M. Yaghi, Weaving of organic threads into a crystalline covalent organic framework, Science 351 (6271) (2016) 365–369.
[3] E. Jin, M. Asada, Q. Xu, S. Dalapati, M.A. Addicoat, M.A. Brady, H. Xu, T. Nakamura, T. Heine, Q. Chen, D. Jiang, Two-dimensional sp^2 carbon–conjugated covalent organic frameworks, Science 357 (6352) (2017) 673–676.
[4] A.P. Côté, A.I. Benin, N.W. Ockwig, M. Keeffe, A.J. Matzger, O.M. Yaghi, Porous, crystalline, covalent organic frameworks, Science 310 (5751) (2005) 1166–1170.
[5] Z. Li, T. He, Y. Gong, D. Jiang, Covalent organic frameworks: pore design and interface engineering, Acc. Chem. Res. 53 (8) (2020) 1672–1685.
[6] N. Keller, T. Bein, Optoelectronic processes in covalent organic frameworks, Chem. Soc. Rev. 50 (3) (2021) 1813–1845.
[7] Z. Wang, S. Zhang, Y. Chen, Z. Zhang, S. Ma, Covalent organic frameworks for separation applications, Chem. Soc. Rev. 49 (3) (2020) 708–735.
[8] R.R. Liang, S.Y. Jiang, A. Ru-Han, X. Zhao, Two-dimensional covalent organic frameworks with hierarchical porosity, Chem. Soc. Rev. 49 (12) (2020) 3920–3951.
[9] S.B. Alahakoon, S.D. Diwakara, C.M. Thompson, R.A. Smaldone, Supramolecular design in 2D covalent organic frameworks, Chem. Soc. Rev. 49 (5) (2020) 1344–1356.
[10] K. Geng, T. He, R. Liu, S. Dalapati, K.T. Tan, Z. Li, S. Tao, Y. Gong, Q. Jiang, D. Jiang, Covalent organic frameworks: design, synthesis, and functions, Chem. Rev. 120 (16) (2020) 8814–8933.
[11] X. Guan, F. Chen, Q. Fang, S. Qiu, Design and applications of three dimensional covalent organic frameworks, Chem. Soc. Rev. 49 (5) (2020) 1357–1384.
[12] B. Gui, G. Lin, H. Ding, C. Gao, A. Mal, C. Wang, Three-dimensional covalent organic frameworks: from topology design to applications, Acc. Chem. Res. 53 (10) (2020) 2225–2234.
[13] H.M. El-Kaderi, J.R. Hunt, J.L. Mendoza-Cortes, A.P. Cote, R.E. Taylor, M. O'Keeffe, O.M. Yaghi, Designed synthesis of 3D covalent organic frameworks, Science 316 (5822) (2007) 268–272.
[14] F.J. Uribe-Romo, J.R. Hunt, H. Furukawa, C. Klöck, M. O'Keeffe, O.M. Yaghi, A crystalline imine-linked 3-D porous covalent organic framework, J. Am. Chem. Soc. 131 (13) (2009) 4570–4571.
[15] G. Lin, H. Ding, D. Yuan, B. Wang, C. Wang, A pyrene-based, fluorescent three-dimensional covalent organic framework, J. Am. Chem. Soc. 138 (10) (2016) 3302–3305.
[16] Y. Zhang, J. Duan, D. Ma, P. Li, S. Li, H. Li, J. Zhou, X. Ma, X. Feng, B. Wang, Three-dimensional anionic cyclodextrin-based covalent organic frameworks, Angew. Chem. Int. Ed. 56 (51) (2017) 16313–16317.
[17] Y. Lan, X. Han, M. Tong, H. Huang, Q. Yang, D. Liu, X. Zhao, C. Zhong, Materials genomics methods for high-throughput construction of COFs and targeted synthesis, Nat. Commun. 9 (1) (2018) 5274.
[18] O. Yahiaoui, A.N. Fitch, F. Hoffmann, M. Froba, A. Thomas, J. Roeser, 3D Anionic silicate covalent organic framework with srs topology, J. Am. Chem. Soc. 140 (16) (2018) 5330–5333.

[19] T. Ma, E.A. Kapustin, S.X. Yin, L. Liang, Z. Zhou, J. Niu, L.-H. Li, Y. Wang, J. Su, J. Li, X. Wang, W.D. Wang, W. Wang, J. Sun, O.M. Yaghi, Single-crystal x-ray diffraction structures of covalent organic frameworks, Science 361 (6397) (2018) 48–52.
[20] H. Li, J. Ding, X. Guan, F. Chen, C. Li, L. Zhu, M. Xue, D. Yuan, V. Valtchev, Y. Yan, S. Qiu, Q. Fang, Three-dimensional large-pore covalent organic framework with stp Topology, J. Am. Chem. Soc. 142 (31) (2020) 13334–13338.
[21] Q. Zhu, X. Wang, R. Clowes, P. Cui, L. Chen, M.A. Little, A.I. Cooper, 3D cage COFs: a dynamic three-dimensional covalent organic framework with high-connectivity organic cage nodes, J. Am. Chem. Soc. 142 (39) (2020) 16842–16848.
[22] H.L. Nguyen, C. Gropp, Y. Ma, C. Zhu, O.M. Yaghi, 3D covalent organic frameworks selectively srystallized through conformational design, J. Am. Chem. Soc. 142 (48) (2020) 20335–20339.
[23] X. Kang, X. Han, C. Yuan, C. Cheng, Y. Liu, Y. Cui, Reticular synthesis of tbo topology covalent organic frameworks, J. Am. Chem. Soc. 142 (38) (2020) 16346–16356.
[24] C. Gropp, T. Ma, N. Hanikel, O.M. Yaghi, Design of higher valency in covalent organic frameworks, Science 370 (6515) (2020) eabd6406.
[25] Z. Li, L. Sheng, H. Wang, X. Wang, M. Li, Y. Xu, H. Cui, H. Zhang, H. Liang, H. Xu, X. He, Three-dimensional covalent organic framework with ceq Topology, J. Am. Chem. Soc. 143 (1) (2021) 92–96.
[26] Y. Xie, J. Li, C. Lin, B. Gui, C. Ji, D. Yuan, J. Sun, C. Wang, Tuning the topology of three-dimensional covalent organic frameworks via steric control: from pts to unprecedented ljh, J. Am. Chem. Soc. 143 (19) (2021) 7279–7284.
[27] H.S. Lu, W.K. Han, X. Yan, C.J. Chen, T. Niu, Z.G. Gu, A 3D anionic metal covalent organic framework with soc topology built from an octahedral Ti(IV) complex for photocatalytic reactions, Angew. Chem. Int. Ed. 60 (33) (2021) 17881–17886.
[28] M. Martinez-Abadia, K. Strutynski, B. Lerma-Berlanga, C.T. Stoppiello, A. N. Khlobystov, C. Marti-Gastaldo, A. Saeki, M. Melle-Franco, A. Mateo-Alonso, π-interpenetrated 3D covalent organic frameworks from distorted polycyclic aromatic hydrocarbons, Angew. Chem. Int. Ed. 60 (18) (2021) 9941–9946.
[29] X. Wang, M. Bahri, Z. Fu, M.A. Little, L. Liu, H. Niu, N.D. Browning, S.Y. Chong, L. Chen, J.W. Ward, A.I. Cooper, A cubic 3D covalent organic framework with nbo topology, J. Am. Chem. Soc. 143 (37) (2021) 15011–15016.
[30] Z. Li, L. Sheng, C. Hsueh, X. Wang, H. Cui, H. Gao, Y. Wu, J. Wang, Y. Tang, H. Xu, X. He, Three-dimensional covalent organic frameworks with hea topology, Chem. Mater. 33 (24) (2021) 9618–9623.
[31] Z. Shan, M. Wu, D. Zhu, X. Wu, K. Zhang, R. Verduzco, G. Zhang, 3D covalent organic frameworks with interpenetrated pcb topology based on 8-connected cubic nodes, J. Am. Chem. Soc. 144 (13) (2022) 5728–5733.
[32] http://rcsr.anu.edu.au/nets.
[33] M.J. Kalmutzki, N. Hanikel, O.M. Yaghi, Secondary building units as the turning point in the development of the reticular chemistry of MOFs, Sci. Adv. 4 (10) (2018) eaat9180.
[34] M.W. Terban, S.J.L. Billinge, Structural analysis of molecular materials using the pair distribution function, Chem. Rev. 122 (1) (2021) 1208–1272.
[35] J. Roeser, D. Prill, M.J. Bojdys, P. Fayon, A. Trewin, A.N. Fitch, M.U. Schmidt, A. Thomas, Anionic silicate organic frameworks constructed from hexacoordinate silicon centres, Nat. Chem. 9 (10) (2017) 977–982.
[36] Y. Liu, Y. Ma, J. Yang, C.S. Diercks, N. Tamura, F. Jin, O.M. Yaghi, Molecular weaving of covalent organic frameworks for adaptive guest inclusion, J. Am. Chem. Soc. 140 (47) (2018) 16015–16019.
[37] Y. Liu, C.S. Diercks, Y. Ma, H. Lyu, C. Zhu, S.A. Alshmimri, S. Alshihri, O.M. Yaghi, 3D covalent organic frameworks of interlocking 1D square ribbons, J. Am. Chem. Soc. 141 (1) (2019) 677–683.
[38] H.-S. Xu, Y. Luo, X. Li, P.Z. See, Z. Chen, T. Ma, L. Liang, K. Leng, I. Abdelwahab, L. Wang, R. Li, X. Shi, Y. Zhou, X.F. Lu, X. Zhao, C. Liu, J. Sun, K.P. Loh, Single crystal of a one-dimensional metallo-covalent organic framework, Nat. Commun. 11 (2020) 1434.
[39] H.S. Xu, Y. Luo, P.Z. See, X. Li, Z. Chen, Y. Zhou, X. Zhao, K. Leng, I.H. Park, R. Li, C. Liu, F. Chen, S. Xi, J. Sun, K.P. Loh, Divergent chemistry paths for 3D and 1D metallo-covalent organic frameworks (COFs), Angew. Chem. Int. Ed. 59 (28) (2020) 11527–11532.
[40] C. Krishnaraj, H. Sekhar Jena, L. Bourda, A. Laemont, P. Pachfule, J. Roeser, C. V. Chandran, S. Borgmans, S.M.J. Rogge, K. Leus, C.V. Stevens, J.A. Martens, V. Van Speybroeck, E. Breynaert, A. Thomas, P., Van Der Voort, Strongly reducing (diarylamino)benzene-based covalent organic framework for metal-free visible light photocatalytic H_2O_2 generation, J. Am. Chem. Soc. 142 (47) (2020) 20107–20116.
[41] S.C. Perry, D. Pangotra, L. Vieira, L.I. Csepei, V. Sieber, L. Wang, C.P. de Leon, F. C. Walsh, Electrochemical synthesis of hydrogen peroxide from water and oxygen, Nat. Rev. Chem. 3 (7) (2019) 442–458.
[42] H. Hou, X. Zeng, X. Zhang, Production of hydrogen peroxide by photocatalytic processes, Angew. Chem. Int. Ed. 59 (40) (2020) 17356–17376.
[43] P. Zhang, D. Sun, A. Cho, S. Weon, S. Lee, J. Lee, J.W. Han, D.-P. Kim, W. Choi, Modified carbon nitride nanozyme as bifunctional glucose oxidase-peroxidase for metal-free bioinspired cascade photocatalysis, Nat. Commun. 10 (1) (2019) 940.
[44] Z. Teng, Q. Zhang, H. Yang, K. Kato, W. Yang, Y.-R. Lu, S. Liu, C. Wang, A. Yamakata, C. Su, B. Liu, T. Ohno, Atomically dispersed antimony on carbon nitride for the artificial photosynthesis of hydrogen peroxide, Nat. Catal. 4 (6) (2021) 374–384.
[45] Y. Isaka, Y. Kawase, Y. Kuwahara, K. Mori, H. Yamashita, Two-phase system utilizing hydrophobic metal-organic frameworks (MOFs) for photocatalytic synthesis of hydrogen peroxide, Angew. Chem. Int. Ed. 58 (16) (2019) 5402–5406.
[46] Q. Wu, J. Cao, X. Wang, Y. Liu, Y. Zhao, H. Wang, Y. Liu, H. Huang, F. Liao, M. Shao, Z. Kang, A metal-free photocatalyst for highly efficient hydrogen peroxide photoproduction in real seawater, Nat. Commun. 12 (2021) 483.
[47] X. Zeng, Y. Liu, Y. Kang, Q. Li, Y. Xia, Y. Zhu, H. Hou, M.H. Uddin, T. R. Gengenbach, D. Xia, C. Sun, D.T. McCarthy, A. Deletic, J. Yu, X. Zhang, Simultaneously tuning charge separation and oxygen reduction pathway on graphitic carbon nitride by polyethylenimine for boosted photocatalytic hydrogen peroxide production, Acs. Catal. 10 (6) (2020) 3697–3706.
[48] X. Chen, X. Peng, L. Jiang, X. Yuan, H. Yu, H. Wang, J. Zhang, Q. Xia, Recent advances in titanium metal–organic frameworks and their derived materials: features, fabrication, and photocatalytic applications, Chem. Eng. J 395 (1) (2020), 125080.
[49] X. Chen, Y. Kuwahara, K. Mori, C. Louisd, H. Yamashita, A hydrophobic titanium doped zirconium-based metal organic framework for photocatalytic hydrogen peroxide production in a two-phase system, J. Mater. Chem. A 8 (4) (2020) 1904–1910.
[50] L. Li, X.S. Wang, T.F. Liu, J. Ye, Titanium-based MOF materials: from crystal engineering to photocatalysis, Small Methods 4 (12) (2020) 2000486.